Gradient catastrophe of nonlinear photonic valley-Hall edge pulses

Daria A. Smirnova,[1,2] Lev A. Smirnov,[2,3] Ekaterina O. Smolina,[2] Dimitris G. Angelakis,[4,5] and Daniel Leykam[4]

[1]*Nonlinear Physics Centre, Australian National University, Canberra ACT 2601, Australia*
[2]*Institute of Applied Physics, Russian Academy of Science, Nizhny Novgorod 603950, Russia*
[3]*Department of Control Theory, Nizhny Novgorod State University, Gagarin Av. 23, Nizhny Novgorod, 603950 Russia*
[4]*Centre for Quantum Technologies, National University of Singapore, 3 Science Drive 2, Singapore 117543*
[5]*School of Electrical and Computer Engineering, Technical University of Crete, Chania, Greece 73100*

(Received 27 February 2021; revised 12 July 2021; accepted 12 August 2021; published 11 October 2021)

We derive nonlinear wave equations describing the propagation of slowly varying wave packets formed by topological valley-Hall edge states. We show that edge pulses break up even in the absence of spatial dispersion due to nonlinear self-steepening. Self-steepening leads to the previously unattended effect of a gradient catastrophe, which develops in a finite time determined by the ratio between the pulse's nonlinear frequency shift and the size of the topological band gap. Taking the weak spatial dispersion into account results in the formation of stable edge quasisolitons. Our findings are generic to systems governed by Dirac-like Hamiltonians and validated by numerical modeling of pulse propagation along a valley-Hall domain wall in staggered honeycomb waveguide lattices with Kerr nonlinearity.

DOI: 10.1103/PhysRevResearch.3.043027

I. INTRODUCTION

The combination of topological band structures with mean-field interactions not only gives rise to rich nonlinear wave physics [1,2] but is also anticipated to unlock advanced functionalities, such as magnet-free nonreciprocity [3], tunable and robust waveguiding [4,5], and novel sources of classical and quantum light [6–11]. Valley-Hall photonic crystals [12–24] show great promise for these applications due to their ability to combine slow-light enhancement of nonlinear effects with topological protection against disorder, which limits the performance of conventional photonic crystal waveguides [25–27].

Accurate modeling of pulse propagation through photonic crystal waveguides in the slow light regime requires taking into account the dispersion in the effective nonlinearity strength, which can induce effects such as pulse self-steepening and supercontinuum generation [28–31]. Despite the proven importance of these effects in applications [32–34], analysis of nonlinear light propagation in topological photonic structures most often assumes nondispersive nonlinearities, in both the underlying material response [35–45] and the effective models describing the propagation of nonlinear edge states [46–50]. The simplest effective model is the cubic nonlinear Schrödinger equation (NLSE), which describes the self-focusing dynamics of edge wave packets independent of the properties of the topological band gap, such as its size.

More sophisticated effective models such as nonlinear Dirac models explicitly include the nontrivial spinlike degrees of freedom required to create topological band gaps [51–55]. In the bulk, the nonlinear Dirac model supports self-induced domain walls and solitons whose stability and degree of localization are sensitive to the gap size. Infinitely extended (plane-wave-like) nonlinear edge states can be obtained analytically and exhibit similar features. However, the nonlinear dynamics of localized edge pulses within the nonlinear Dirac model framework were not yet considered.

In this paper we study an analytically solvable nonlinear Dirac model (NDM) describing topological edge pulses, revealing that nonlinear topological edge states exhibit a self-steepening nonlinearity when the pulse self-frequency modulation becomes comparable to the width of the topological band gap. The self-steepening nonlinearity leads to the formation of a gradient catastrophe of edge wave packets within a finite propagation time proportional to the pulse width. Taking the weak spatial dispersion of the topological edge modes into account regularizes the catastrophe and results in the formation of stable edge solitons for sufficiently long pulses. We validate our analysis using numerical simulations of beam propagation in a laser-written valley-Hall waveguide lattice, demonstrating that this effect should be observable even for relatively weak nonlinearities. Our findings suggest valley-Hall photonic crystal waveguides will provide a fertile setting for observing and harnessing higher-order nonlinear optical effects.

II. Nonlinear Dirac Model

We consider a generic continuum Dirac model of topological photonic lattices with incorporated nonlinear terms. The evolution of a spinor wave-function $\mathbf{\Psi}(x, y, t) = [\Psi_1(x, y, t); \Psi_2(x, y, t)]^T$ in the vicinity of a band crossing point (topological phase transition) is governed by the

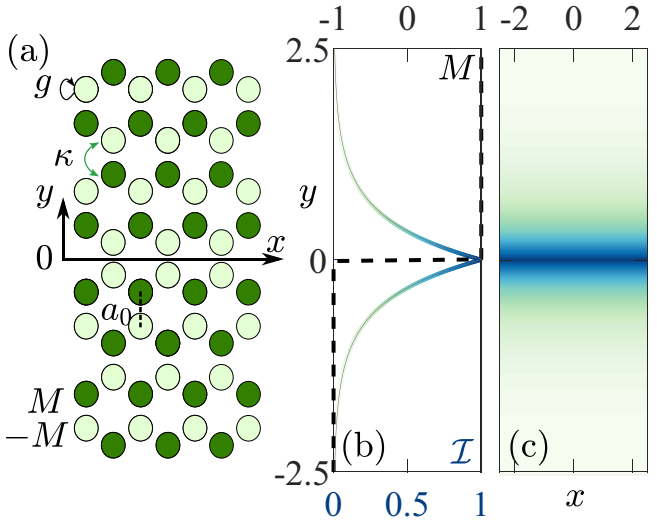

FIG. 1. (a) Dimerized photonic graphene lattice with staggered sublattice potential. Here κ denotes the tunneling coefficient between waveguides, a_0 is the distance between neighboring waveguides, and the round arrow g illustrates the nonlinear self-action effect. (b) Transverse profile $\mathcal{I}(y)$ and (c) in-plane intensity distribution $\mathcal{I}(x, y) = |\psi_1(x, y)|^2 + |\psi_2(x, y)|^2$ of the nonlinear edge wave propagating along the x axis and bound to the domain wall located at $y = 0$, where the effective mass $M(y)$ changes sign. Parameters are $M_0 = 1$, g $= 0.75$.

nonlinear Dirac equation [51,54,55]

$$i\partial_t \boldsymbol{\Psi} = (\hat{H}_D(\delta\mathbf{k}) + \hat{H}_{NL})\boldsymbol{\Psi}; \tag{1}$$

$$\hat{H}_D(\delta\mathbf{k}) = \delta k_x \hat{\sigma}_x + \delta k_y \hat{\sigma}_y + M\hat{\sigma}_z, \tag{2}$$

where $\delta\mathbf{k} = (\delta k_x, \delta k_y) \equiv -i(\partial_x, \partial_y)$ is the momentum, M is a detuning between two sublattices or spin states, and $\hat{H}_{NL} = -g\,\mathrm{diag}[|\Psi_1|^2; |\Psi_2|^2]$ is a local nondispersive Kerr nonlinearity.

As a specific example, the model (1) can be implemented in nonlinear photonic graphene with a staggered sublattice potential as illustrated in Fig. 1(a). A dimerized graphene lattice is composed of single-mode dielectric waveguides with local Kerr nonlinearity. The effective mass M characterizes a detuning between propagation constants in the waveguides of two sublattices. The form of Hamiltonian operator (2) assumes normalization of the transverse coordinates x, y and evolution variable in the propagation direction $t \sim z/v_D$ to the Dirac velocity $v_D = 3\kappa a_0/2$ defined by the lattice parameters, a coupling constant κ and a distance a_0 between two neighboring waveguides [23,55]. This continuum model is valid provided $|\kappa| \gtrsim 2|M|$ [23].

The *valley-Hall domain wall* is created between two insulators characterized by different signs of the mass. We take a signum distribution,

$$M(y) = \begin{cases} M_0, & y > 0, \\ -M_0, & y < 0, \end{cases} \tag{3}$$

and without loss of generality assume $M_0 > 0$ in the upper half-space. In the lattice model, mass inversion corresponds to interfacing two honeycomb lattices with opposite parity breaking [16,23,56]. The domain wall hosts chiral valley edge states whose origin in the linear case can be traced to the general principle of bulk-boundary correspondence and a difference of ± 1 between valley Chern numbers across a domain wall [57,58]. Being defined by bulk properties, such edge states are robust to relatively small perturbations precluding intervalley mixing. Modifications of the bulk spectrum in the nonlinear regime, including the nonlinear Dirac cone bifurcation, are discussed in Refs. [52,59]. The valley Chern number formally stays the same as its linear counterpart until the upper band of nonlinear Bloch waves forms a self-crossing loop at above-threshold bulk intensities $g\mathcal{I} \geqslant 2M_0$ [52].

In Ref. [55] we derived exact analytic solutions for the propagating nonlinear valley edge modes bound to the interface $y = 0$: $\boldsymbol{\Psi}(y, x, t) = [\psi_1^0(y, \omega, k); \psi_2^0(y, \omega, k)]^T e^{ikx - i\omega t}$. These nonlinear edge states originate from their linear counterparts. Based on the close connections between nonlinear edge states and self-trapped Dirac solitons in topological band gaps revealed in Ref. [55], the nonlinear edge mode dispersion can be obtained as

$$\omega + k = -g\mathcal{I}_1/2, \tag{4}$$

with the transverse profile of the edge state determined by the intensity at the interface $\mathcal{I}_1 = |\psi_{1,2}(y = 0)|^2$ (see Appendix A). In Figs. 1(b) and 1(c) we show the plane-wave-like profile of the nonlinear edge mode with fixed wave-number k parallel to the edge.

III. EDGE PULSE DYNAMICS

Now we consider the dynamics of finite edge pulses constructed as a superposition of the valley edge modes. Using the global parity symmetry with respect to the interface and analytical solutions for the edge states (see Appendix A), we calculate two characteristics of the edge states via integration in the upper half plane $y > 0$: the power $\mathcal{P}$ and the spin S_x,

$$\mathcal{P} = \int_0^\infty \boldsymbol{\psi}^\dagger \boldsymbol{\psi} dy, \quad S_x = \frac{1}{2}\int_0^\infty \boldsymbol{\psi}^\dagger \hat{\sigma}_x \boldsymbol{\psi} dy\,, \tag{5}$$

and identify a functional relation $S_x(\mathcal{P})$ between them:

$$S_x = -\frac{1}{g}\arcsin\left[\frac{1}{\sqrt{2}}\sin\left(\mathcal{P}\frac{g}{\sqrt{2}}\right)\right]. \tag{6}$$

Crucially, this relation is independent of the wave-vector k, which allows us to develop a slowly varying envelope approximation to describe the nonlinear dynamics of finite edge wave packets. Using Eq. (1), it can be shown that the integral characteristics obey the following evolution equation:

$$\partial_t \mathcal{P} = -2\partial_x S_x(\mathcal{P}). \tag{7}$$

Next, we assume $\mathcal{P}(x, t)$ and $S_x(x, t)$ are slowly varying functions of the local frequency and wave number, such that Eq. (6) remains valid to a first approximation for smooth x-dependent field envelopes. Plugging Eq. (6) into Eq. (7), and using Eq. (4) assuming weak nonlinearity $g\mathcal{I}_1 \ll M_0$, we obtain the simple nonlinear wave equation for the longitudinal intensity profile $\mathcal{I}_1(x, t)$:

$$\partial_t \mathcal{I}_1 - \partial_x \mathcal{I}_1\left(1 - g^2\mathcal{I}_1^2/\left(4M_0^2\right)\right) = 0. \tag{8}$$

Equation (8) suggests that the evolution of finite wave packets propagating along the x axis is accompanied by steepening of

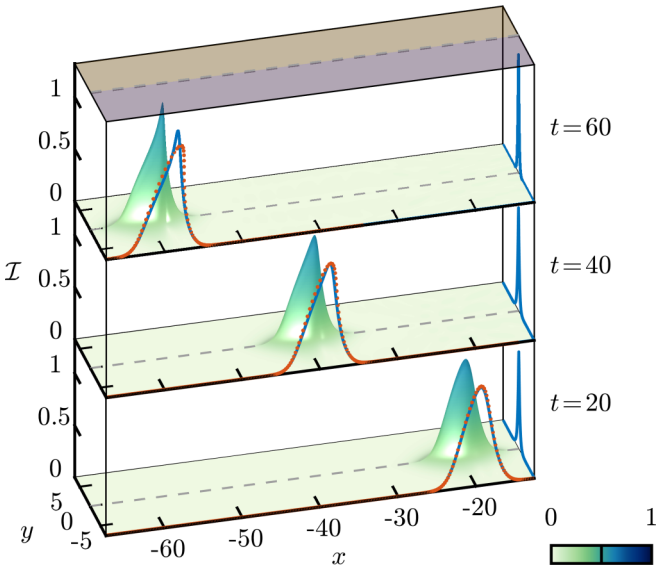

FIG. 2. Gradient catastrophe development. The Gaussian pulse with $F_0 = 0.5$, $\Lambda_0 = 3.5/\sqrt{2}$ is launched at $t = 0$. Slices color code intensity distributions $\mathcal{I}(x, y)$ at the given moments: $t = 20$ (bottom), $t = 40$ (middle), $t = 60$ (top). Cuts along the domain wall at $y = 0$ show consistency of the numerical solution (blue curves) with the solution of the nonlinear simple wave equation (8) for the intensity (red dotted lines). Parameters are $M_0 = 1$, $g = 0.75$, $gF_0 = 0.375M_0$. In Figs. 2 and 3, dashed lines trace the domain wall separating spatial domains with masses of the opposite sign as indicated by shading with different colors on the top surface. The theoretical estimate of breakdown time $t^* \approx 58$ according to formula (10) perfectly matches the numerical scenario.

the trailing wave front up to the development of a *gradient catastrophe*. Note that in the linear case $g = 0$, Eq. (8) shows that the edge wave packet of any shape does not diffract and propagates along the domain wall with constant group velocity $v = -1$ being granted with topological robustness. If $M_0 < 0$, the group velocity is positive, and a pulse propagates in the opposite direction.

Alternatively, Eq. (8) can be derived using asymptotic methods based on a series expansion of the spinor wave function [see Appendix B],

$$\Psi_{1,2}(x, y, t) = \pm a(\xi; \tau_1, \tau_2, \ldots)e^{-M_0|y|} + \sum_{n=1}^{\infty} \mu^n \Psi_{1,2}^{(n)}(y; \xi; \tau_n), \tag{9}$$

where we have introduced a small parameter $\mu \sim g\mathcal{I}_1/M_0$, a hierarchy of time scales $\tau_n = \mu^n t$, and assumed a smooth dependence of the spinor components on t in the moving coordinate frame ($\xi \equiv x + t, y$).

To illustrate the key effect of the gradient catastrophe captured by Eq. (8), we model the time dynamics of an edge wave packet using a custom numerical code, applying a split-step scheme and the fast Fourier transform to solve Eq. (1). Figure 2 shows the evolution of the initial distribution set in the form of the edge state across the interface with the Gaussian envelope $\mathcal{I}_1^0(x, t = 0) = F_0 e^{-x^2/\Lambda_0^2}$ along the x axis: $\boldsymbol{\psi}(y, x, t = 0) = [\psi_1^0(y, \omega = -g\mathcal{I}_1^0(x)/2, 0); \psi_2^0(y, \omega = -g\mathcal{I}_1^0(x)/2, 0)]^T$. Plugging the Gaussian distribution into Eq. (8), we may estimate the pulse breakdown time t_* analytically by the method of characteristics:

$$t_* = 2\sqrt{e}\Lambda_0 \left(\frac{M_0}{gF_0}\right)^2. \tag{10}$$

Thus, pulse breakdown occurs for finite wave packets when the peak nonlinear frequency shift becomes comparable to the size of the topological band gap. As the pulse propagates, its tail becomes increasingly steep, developing a discontinuity (i.e., a shock) in a finite time. The numerical solution of Eq. (1) is fully consistent with our analytical considerations; see Fig. 2.

IV. SPATIAL DISPERSION EFFECT AND ENVELOPE EQUATION

Weak spatial dispersion effects serve as a possible mechanism regularizing the gradient catastrophe, resulting in the formation of solitons. For honeycomb photonic lattices, dispersion is accounted for by introducing off-diagonal second-order derivatives with the coefficient $\eta = 3\kappa a_0^2/(8v_D^2) = (6\kappa)^{-1}$ into the Dirac model (1):

$$\hat{H}_{\text{disp}} = \begin{pmatrix} 0 & -\eta(-i\partial_x + \partial_y)^2 \\ -\eta(i\partial_x + \partial_y)^2 & 0 \end{pmatrix}. \tag{11}$$

Assuming $\eta M_0 \sim \mu^2$ and developing a perturbation theory with expansion (9), we derive an evolution equation governing the complex-valued amplitude $a(\xi, t)$:

$$i\left(\partial_t a + \frac{g^2|a|^2}{32M_0^2} a\partial_\xi |a|^2\right) + \frac{g}{4}|a|^2 a + \eta\left(\partial_{\xi\xi} a - M_0^2 a\right) = 0, \tag{12}$$

which differs from the conventional cubic NLSE by the second higher-order nonlinear term responsible for the phase modulation and self-steepening.

Equation (12) enables analysis of both the modulational instability of nonlinear plane-wave-like edge states and the formation of edge quasisolitons (see Appendix B). Importantly, earlier works on edge solitons [36,48–50] were limited to considerations based on reducing dynamics to the effective one-dimensional NLSE, which exhibits instabilities and bright solitons in the case of attractive interactions. The standard NLSE, however, is completely independent of the topological band-gap properties. In contrast, Eqs. (8) and (12), derived from the vectorial Dirac equations in full compliance with each other, show that edge pulses in topological systems can break even in the absence of spatial dispersion due to nonlinear self-steepening.

In the mathematical aspect, Eqs. (4), (7), (8), and (12), written for different quantities, are fully consistent with each other. For instance, bearing in mind $\sqrt{2\mathcal{I}_1} \equiv |a|$, Eqs. (4) and (8) can be straightforwardly recovered from Eq. (12) at $\eta = 0$ in the first and second order of perturbation theory, respectively (see also Sec. 2 of Appendix B). In turn, plugging a multiscale expansion for the spinor function (9) into Eq. (7) yields Eq. (12) at $\eta = 0$.

To verify the validity of the modified NLSE (12), we consider the propagation of a Gaussian pulse in Fig. 3. The conventional NLSE, which lacks the self-steepening term,

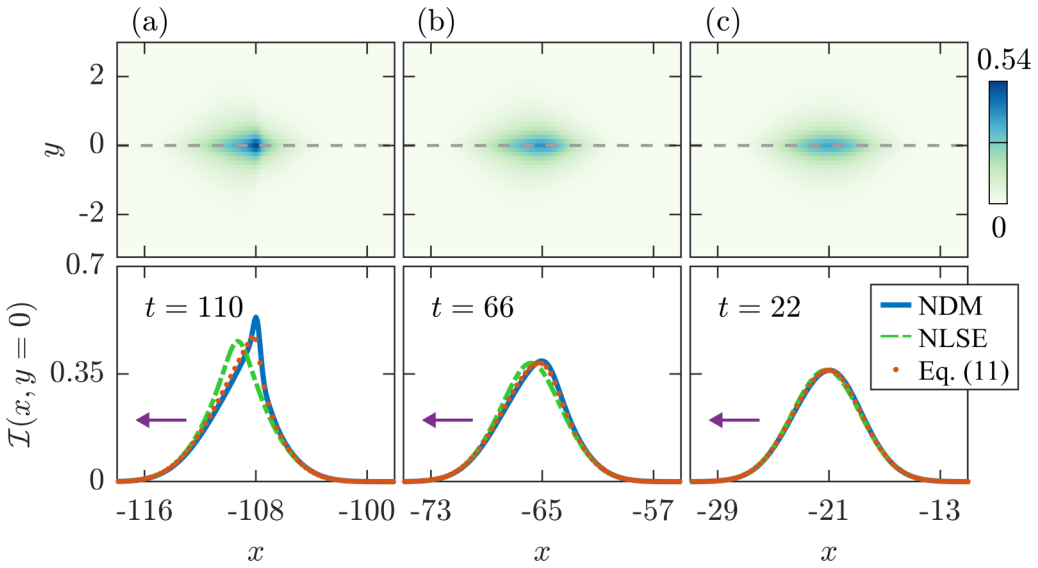

FIG. 3. Nonlinear pulse transformation in the domain-wall problem with dispersion. Snapshots show intensity distributions in-plane $\mathcal{I}(x, y)$ (top row) and along the domain wall $\mathcal{I}(x, y = 0)$ (bottom row) at the given times: (a) $t = 110$, (b) $t = 66$, (c) $t = 22$. Overlaid curves are the pulse envelopes calculated by using NLSE (green dashed) and Eq. (12) (red dotted). The Gaussian pulse with $F_0 = 0.18$, $\Lambda_0 = 5/\sqrt{2}$ is launched at $t = 0$. Parameters are $M_0 = 1$, $g = 1$, $\eta = 0.001$.

only exhibits self-focusing and gradual self-compression of the pulse. On the other hand, the modified Eq. (12) correctly reproduces the growing asymmetry of the edge pulse as it propagates. Note also that in Fig. 2, which neglects spatial dispersion with $\eta = 0$, up to the gradient catastrophe the peak intensity of the pulse stays the same, in agreement with the nonlinear simple wave equation (8). In contrast, the peak intensity in Fig. 3 grows due to self-focusing behavior induced by the spatial dispersion term.

V. PULSE BREAKDOWN AND SOLITON FORMATION

We now consider the dynamics of wide edge pulses beyond the breakdown time t_*, taking weak spatial dispersion into account. Figure 4 illustrates the long time propagation dynamics of an edge pulse. The gradient catastrophe is visible in Fig. 4(b) as a very large intensity derivative at the trailing end of the pulse. This is accompanied by an increase in the peak wave-packet intensity, resulting in a violation of the weak nonlinearity condition $g\mathcal{I}_1 < M_0$ and the resonant coupling of energy into bulk modes in Fig. 4(d). The pulse breaks down into a wave packet comprising multiple peaks.

The wave packet continues to radiate energy until at long times it relaxes to a single weakly nonlinear edge soliton which preserves its shape as it continues to propagate along the domain wall [Figs. 4(a) and 4(b)], as predicted by our perturbative analysis. Such solitons can be obtained in Eq. (12); they exhibit stable propagation and are capable of traversing sharp bends (see Sec. 3 of Appendix B). We note that even after the initial pulse breakup, self-steepening terms can influence the soliton stability and soliton-soliton interactions [32].

VI. WAVEGUIDE ARRAY IMPLEMENTATION

In this section we show how our models can describe light propagation in nonlinear waveguide arrays governed by

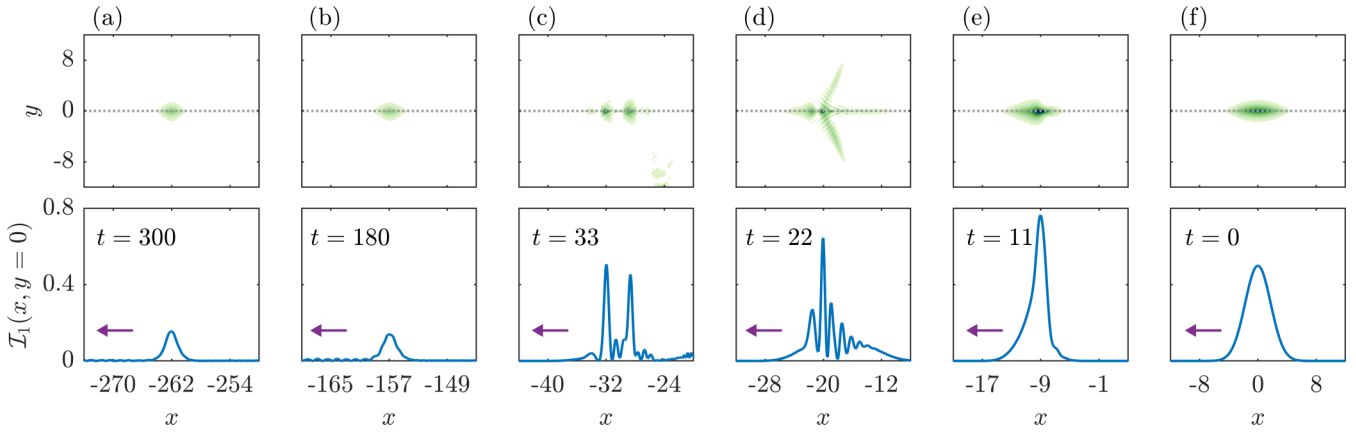

FIG. 4. Formation of solitonic edge pulses. Upper row: Snapshots of the in-plane field distribution $|\psi_1|^2(x, y)$ at the given times: (a) $t = 300$, (b) $t = 180$, (c) $t = 33$, (d) $t = 22$, (e) $t = 11$, (f) $t = 0$. Lower row: Field profiles $|\psi_1|^2(x, y = 0)$ along the domain wall located at $y = 0$. The direction of propagation is to the left. Parameters are $M_0 = 1$, $g = 1$, $\eta = 0.05$, $F_0 = 0.5$, $\Lambda_0 = 3.5/\sqrt{2}$.

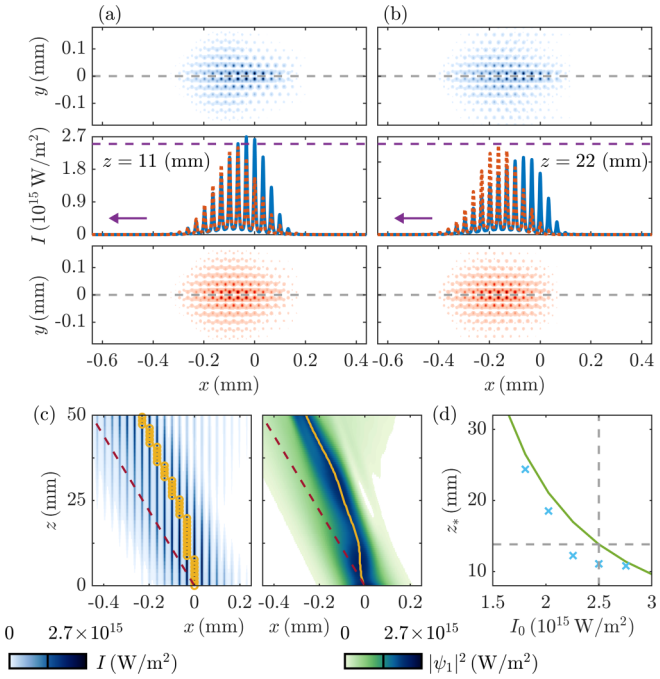

FIG. 5. Nonlinear dynamics of the optical beam at the valley-Hall domain wall at a zigzag interface in a honeycomb lattice of laser-written waveguides. The input beam has a Gaussian envelope along the domain wall with maximum intensity $I_0 = 2.5 \times 10^{15}$ W/m^2. (a), (b) Intensity distributions of the nonlinear beam (top panels, blue line) at propagation distances (a) $z = 11$ mm (left column) and (b) $z = 22$ mm (right column). For comparison, the linear beam evolution, i.e., with nonlinearity switched off, is shown in the bottom panels and with dotted red lines. Purple arrows points to the direction of motion. Dashed gray line depicts the domain wall. (c) Intensity distribution at the interface obtained in modeling of the paraxial equation (left) and the corresponding Dirac model (right). The purple dashed line traces a straight trajectory of the center of mass of the linear pulse. (d) Breakdown coordinate z_* as a function of the input intensity I_0 estimated from the Dirac model (green curve) and paraxial modeling (cyan crosses). The dashed gray lines' intersection indicates the value of the input beam intensity used for (a), (b), and (c).

the well-established paraxial equation, without requiring any tight-binding or continuum Dirac model approximations. As a possible implementation, we consider a realistic valley-Hall waveguide array of laser-written waveguides with parameters similar to those used in the experimental work in Ref. [16]. In this case, the evolution variable t becomes the longitudinal propagation distance z.

To simulate the evolution, we solve the paraxial equation numerically in a periodic potential by propagating an optical wave packet (see Appendix C). For realistic laser input powers, we observe a rapidly developing self-steepening of the beam envelope in Figs. 5(a) and 5(b). Figure 5(c) additionally shows the intensity map in the xz interface plane. Note that here the catastrophe itself is smoothed out due to the spatial dispersion.

To compare the paraxial dynamics against the self-steepening time scale Eq. (10) predicted by the simple nonlinear wave equation, we use the time required for the peak derivative of the pulse envelope to double in magnitude as an estimate of the self-steepening time. This peak derivative doubling time is plotted as a function of the peak input intensity as blue crosses in Fig. 5(d). The pulse breakdown time provided by the simple wave equation (solid line) provides a good approximation of this self-steepening time scale. Moreover, this time scale is clearly much smaller than the time required for regular modulational instability to develop, given that the pulse profile remains smooth.

Thus, our theory predicts that the dominant nonlinear effect for valley Hall edge pulses is self-steepening, rather than modulational instability, which was previously assumed based on analysis of plane-wave-like edge states. This is our key result. We also checked numerically that linear and nonlinear evolution of the edge beam depicted in Figs. 5(a) and 5(b) does not significantly change upon introducing a defect created by a missing waveguide, which hints at the robustness of the self-steepening dynamics of pulses constructed from topological edge states.

VII. CONCLUSION

In conclusion, we have described the gradient catastrophe of the nonlinear edge wave packets in the spinor-type Dirac equation and the formation of edge solitons at the valley-Hall domain walls. We have derived a higher-order self-steepening NLSE describing these effects. Spatiotemporal numerical modeling confirmed that pulse self-steepening can manifest already in the framework of paraxial optics in weakly nonlinear media, such as topological waveguide lattices, and will likely play a key role in future experiments with topological photonic crystal waveguides. Beyond the specific valley-Hall example we considered, our findings are instructive for other emerging experimental studies of nonlinear dynamic phenomena in topological systems, such as the Chern insulators and their implementations in a variety of physical platforms spanning from metamaterials [4] to optical lattices [43,44] and exciton-polariton condensates [60].

ACKNOWLEDGMENTS

This work was supported by the Australian Research Council (Grant No. DE190100430), the Russian Foundation for Basic Research (Grants No. 19-52-12053 and No. 19-02-00261), the National Research Foundation, Prime Minister's Office, Singapore; the Ministry of Education, Singapore, under the Research Centres of Excellence programme; and the Polisimulator project co-financed by Greece and the EU Regional Development Fund. Theoretical analysis of the continuum model was supported by the Russian Science Foundation (Grant No. 20-72-00148). D.A.S. thanks Yuri Kivshar for valuable discussions.

APPENDIX A: NONLINEAR EDGE STATES

In Ref. [55], we derived analytical solutions for gap soliton stripes of the form $\Psi_{1,2} = \psi_{1,2}(y,t)e^{ikx}$ in the continuum nonlinear $(2+1)$ Dirac model (1) with a uniform mass distribution $M(x,y) = M_0 = \text{const}$. The transverse structure of the standing soliton is expressed through spin angle $\alpha_s(y)$ and

intensity $\varrho_s(\alpha_s(y))$,

$$\begin{pmatrix} \psi_1(y,t) \\ \psi_2(y,t) \end{pmatrix} = \sqrt{2\varrho_s(y)} \begin{pmatrix} \cos\alpha_s(y) \\ -\sin\alpha_s(y) \end{pmatrix} e^{-i\omega t}. \tag{A1}$$

The spin angle $\alpha_s(y) \equiv \alpha_n - \delta/2$ is defined through auxiliary variables α_n, δ, Ω:

$$\begin{aligned} \alpha_n(y) &= \tan^{-1}\left[\frac{\Omega-\omega}{\sqrt{\Omega^2-\omega^2}}\tanh(\sqrt{\Omega^2-\omega^2}\,y)\right], \\ \delta &= \tan^{-1}\frac{k}{M_0}, \quad \Omega = \sqrt{M_0^2+k^2}, \\ \sin\delta &= \frac{k}{\Omega}, \quad \cos\delta = \frac{M_0}{\Omega}. \end{aligned} \tag{A2}$$

With the use of formulas (A2), the intensity ϱ_s is found as

$$\begin{aligned} \varrho_s(\alpha_s(y)) &= \frac{2(\Omega\cos 2\alpha_n - \omega)}{g(1+\cos^2 2\alpha_s)} = \frac{2}{g}\frac{d\alpha_s/dy}{(1+\cos^2 2\alpha_s)} \\ &= \frac{2(-k\sin 2\alpha_s - \omega + M_0\cos 2\alpha_s)}{g(1+\cos^2 2\alpha_s)}. \end{aligned} \tag{A3}$$

Note, due to translational invariance, replacement of y with $(y+y_0)$, where y_0 is an arbitrary coordinate shift, in expressions (A2), (A3) also yields a solution.

The gap soliton stripe solution can be used to construct nonlinear modes supported by topological interfaces formed by domain walls of the mass (3), where the interface at $y=0$ separates two half-spaces. Based on the global parity symmetry of the system with respect to the interface, the effective boundary condition relates the two components of the spinor as

$$\psi_1(y=0) = \mp\psi_2(y=0), \tag{A4}$$

where the sign $-/+$ corresponds to the positive/negative M_0. We rewrite the boundary condition (A4) in terms of the spin angle:

$$\alpha_s(0) = \pm\pi/4. \tag{A5}$$

In the linear case, Eq. (A5) yields antisymmetric or symmetric spinors, [1, −1] or [1,1], of edge states with the linear dispersion $\omega = \mp k$.

The nonlinear edge states can then be retrieved from the gap stripe soliton solutions, as illustrated in Fig. 6. The dispersion relation for edge solitons (4) follows from Eq. (A3) and the boundary condition Eq. (A5). By contrast to the linear case, it depends on the intensity. The boundary coordinate y_0 is determined from the boundary condition using Eq. (A2), where $y \to (y+y_0)$:

$$\begin{aligned} \tanh(\sqrt{\Omega^2-\omega^2}\,y_0) &= \sqrt{\frac{\Omega+\omega}{\Omega-\omega}}\tan\left(\pm\frac{\pi}{4}+\frac{\delta}{2}\right) \\ &\equiv \sqrt{\frac{\Omega+\omega}{\Omega-\omega}}\left(\frac{\pm1+\tan\frac{\delta}{2}}{1\mp\tan\frac{\delta}{2}}\right). \end{aligned} \tag{A6}$$

Besides, from (A2) we can express $y(\alpha_s)$ as a function of the spin angle:

$$y = \frac{1}{\sqrt{\Omega^2-\omega^2}}\tan^{-1}\left(\sqrt{\frac{\Omega+\omega}{\Omega-\omega}}\tan\left(\alpha_s+\frac{\delta}{2}\right)\right) - y_0. \tag{A7}$$

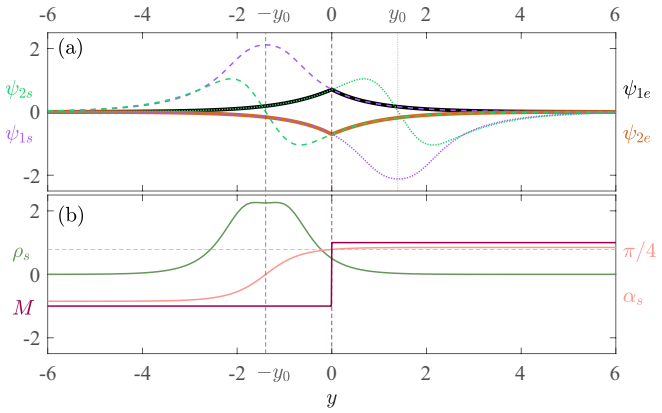

FIG. 6. (a) Profiles of the nonlinear edge state's components ψ_{1e} (solid black) and ψ_{2e} (solid brown) confined to the domain wall at $y=0$. The transverse structure of the standing soliton (A1) shifted by $(-/+y_0)$ with components ψ_{1s} (dashed/dotted violet) and ψ_{2s} (dashed/dotted green) determines the structure of the nonlinear edge state in the positive/negative half-space. (b) Spin angle $\alpha_s(y)$ (pink curve) and intensity $\varrho_s(\alpha_s(y))$ (green curve) for the soliton shifted by $(-y_0)$ to the left of the domain wall. Purple line depicts the steplike mass distribution $M(y)$. Parameters are $M_0 = 1$, $\mathcal{I}_1 \equiv |\psi_{1e}(0)|^2 = |\psi_{2e}(0)|^2 = 0.5$, $g = 0.5$, $k = 0$.

In the semi-infinite interval, $y = [0,\infty]$, α_s monotonously changes from $\alpha_s(0)$ to

$$\alpha_s(\infty) = -\frac{\delta}{2} + \tan^{-1}\left[\frac{\sqrt{\Omega-\omega}}{\sqrt{\Omega+\omega}}\right]. \tag{A8}$$

Next, according to Eq. (5), we define the integral characteristics of nonlinear edge states—power $2\mathcal{P}$ and spin $2S_x$. In the upper half-space, $y > 0$, the total power is calculated as

$$\mathcal{P} = \int_{y_0}^{\infty} 2\rho(\alpha_s(y))dy = \int_{\alpha_s(0)}^{\alpha_s(\infty)} \rho(\alpha_s)\frac{\partial y}{\partial\alpha_s}d\alpha_s, \tag{A9}$$

where we substitute the expression for $\rho_s \propto d\alpha_s/dy$ from Eq. (A3). As a result of integration we get

$$\mathcal{P} = \frac{\pi}{g\sqrt{2}} + \frac{\sqrt{2}}{g}\tan^{-1}\left(\frac{-k\omega + M_0\sqrt{\Omega^2-\omega^2}}{\sqrt{2}[M_0\omega + k\sqrt{\Omega^2-\omega^2}]}\right). \tag{A10}$$

Thus, the edge state's power depends on both its intensity via the intensity dependence of the nonlinear dispersion Eq. (4) and its profile along the edge via the wave-number k. Similarly, we calculate the integral spin:

$$\begin{aligned} S_x &= -\int_0^{\infty} \varrho_s \sin(2\alpha_s)dy \\ &= \frac{1}{g}\tan^{-1}\left(\frac{M_0\omega + k\sqrt{\Omega^2-\omega^2}}{\Omega^2}\right). \end{aligned} \tag{A11}$$

Remarkably, there exists a k-independent functional connection between these two integral characteristics:

$$\cos\left(\left(\mathcal{P} - \frac{\pi}{g\sqrt{2}}\right)\frac{g}{\sqrt{2}}\right) = \sqrt{2}|\sin gS_x|. \tag{A12}$$

For relatively weak nonlinearity, Eq. (A12) is simplified to:

$$\mathcal{P} = \frac{\pi}{g\sqrt{2}} - \frac{\sqrt{2}}{g}\arccos(-\sqrt{2}\sin gS_x), \tag{A13a}$$

$$S_x = -\frac{1}{g}\arcsin\left[\frac{1}{\sqrt{2}}\sin\left(\mathcal{P}\frac{g}{\sqrt{2}}\right)\right]. \tag{A13b}$$

In the case $g\mathcal{P} \to 0$, we recover an asymptotic transition to the case of a linear edge state:

$$\mathcal{P} = \frac{\mathcal{I}_1}{M}, \tag{A14a}$$

$$S_x = -\frac{1}{2}\mathcal{P}. \tag{A14b}$$

In the linear limit $M_0 y_0 \gg 1$ ($M_0 > 0$), the edge state solution is converted to the conventional form—an antisymmetric spinor with $\omega = -k$:

$$\begin{pmatrix} \Psi_1(x,y,t) \\ \Psi_2(x,y,t) \end{pmatrix} = \sqrt{\frac{2M_0}{g}} e^{-M_0|y+y_0|} \begin{pmatrix} 1 \\ -1 \end{pmatrix} e^{-i\omega t - ikx}. \tag{A15}$$

To obtain explicit approximate expressions for the integral characteristics in the limit of weak nonlinearity, we use the perturbation theory developed in Appendix B, Sec. 2. In the perturbative limit, the edge state profile of amplitude $a_0 = \sqrt{2\mathcal{I}_1}$ for $y > 0$ is

$$\psi_1 \approx \frac{1}{\sqrt{2}} a_0 \left[e^{-M_0 y} - \frac{g a_0^2}{8M_0}(e^{-M_0 y} - e^{-3M_0 y}) \right], \tag{A16a}$$

$$\psi_2 \approx -\frac{1}{\sqrt{2}} a_0 \left[e^{-M_0 y} + \frac{g a_0^2}{8M_0}(e^{-M_0 y} - e^{-3M_0 y}) \right], \tag{A16b}$$

corresponding to the power

$$\mathcal{P} \approx \frac{a_0^2}{2M_0}\left[1 + \frac{1}{3}\left(\frac{g a_0^2}{8M_0}\right)^2\right] \tag{A17}$$

and integral spin

$$S_x \approx -\frac{1}{2}\left(\frac{a_0^2}{2M_0}\right)\left[1 - \frac{1}{3}\left(\frac{g a_0^2}{8M_0}\right)^2\right]. \tag{A18}$$

We can also obtain the edge state's mean displacement from the edge $\langle y \rangle$, which is related to its transverse localization length $\mathcal{Y} = \int_0^\infty \boldsymbol{\psi}^\dagger \boldsymbol{\psi} y dy$:

$$\mathcal{Y} \approx \frac{1}{2M_0}\left(\frac{a_0^2}{2M_0}\right)\left[1 + \frac{11}{18}\left(\frac{g a_0^2}{8M_0}\right)^2\right], \tag{A19a}$$

$$\langle y \rangle = \mathcal{Y}/\mathcal{P} \approx \frac{1}{2M_0}\left[1 + \frac{5}{18}\left(\frac{g a_0^2}{8M_0}\right)^2\right]. \tag{A19b}$$

APPENDIX B: NONLINEAR DYNAMICS OF EDGE PULSES

1. Derivation of the nonlinear simple wave equation

We write out the NDM (1) for the evolution of the spinor wave-function $\boldsymbol{\Psi}(x,y,t) = [\Psi_1(x,y,t); \Psi_2(x,y,t)]^T$ together with its complex conjugate pair:

$$i\frac{\partial \Psi_1}{\partial t} = (-i\partial_x - \partial_y)\Psi_2 + M\Psi_1 - g|\Psi_1|^2\Psi_1, \tag{B1a}$$

$$i\frac{\partial \Psi_2}{\partial t} = (-i\partial_x + \partial_y)\Psi_1 - M\Psi_2 - g|\Psi_2|^2\Psi_2, \tag{B1b}$$

$$-i\frac{\partial \Psi_1^*}{\partial t} = (i\partial_x - \partial_y)\Psi_2^* + M\Psi_1^* - g|\Psi_1|^2\Psi_1^*, \tag{B1c}$$

$$-i\frac{\partial \Psi_2^*}{\partial t} = (i\partial_x + \partial_y)\Psi_1^* - M\Psi_2^* - g|\Psi_2|^2\Psi_2^*. \tag{B1d}$$

Multiply (B1a) by Ψ_1^*, (B1b) by Ψ_2^*, (B1c) by Ψ_1, and (B1d) by Ψ_2. Then we subtract the third (fourth) of the obtained relations from the first (second) one, sum up the two resultant expressions, and integrate over y in infinite limits. The left-hand side of the integral equation is transformed to a derivative of the power $i\partial_t \mathcal{P}(x,t)$. The right side contains a derivative of the spin and equals $-2i\partial_x S_x(x,t)$. The rest of the terms in the right-hand side do not contribute to the integral for localized solutions $\Psi_{1,2}$, such as edge states bound to the domain wall at $y = 0$. This can be shown integrating by parts. As a result of the above transformations, we obtain the evolution equation for the integral characteristics of the transversely localized solutions Eq. (7).

We can solve Eq. (7) by considering an edge pulse with an envelope that is slowly varying in time and space. In such pulses, over sufficiently long propagation distances the transverse wave structure locally is weakly deviated from the edge mode profile described in Appendix A. Therefore, we may approximately employ expressions (A10), (A11) for $\mathcal{P}$ and S_x, considering them as functions of the local instantaneous frequency $\omega(t,x)$ and local instantaneous wave number $k(t,x)$, defined as

$$\omega = -\frac{\partial \varphi}{\partial t}, \quad k = \frac{\partial \varphi}{\partial x}, \tag{B2}$$

where $\varphi(t,x)$ is a distribution of the phase in the pulse over the domain wall located at $y = 0$. Definitions (B2) yield the relation

$$\partial_x \omega = -\partial_t k. \tag{B3}$$

Using formulas from Appendix A, we calculate the derivatives $\partial_t \mathcal{P}(\omega(t,x), k(t,x))$, $\partial_x S_x(\omega(t,x), k(t,x))$ entering (7) and substitute them into Eq. (7) to get

$$\frac{\partial \alpha_s(\infty)}{\partial \omega}\left(\frac{\partial \omega}{\partial t} - \frac{\partial \omega}{\partial x}\sin 2\alpha_s(\infty)\right) + \frac{\partial \alpha_s(\infty)}{\partial k}\left(\frac{\partial k}{\partial t} - \frac{\partial k}{\partial x}\sin 2\alpha_s(\infty)\right) = 0. \tag{B4}$$

Taking into account Eq. (A2), three quantities in Eq. (B4) can be expressed through ω and k:

$$\frac{\partial \alpha_s(\infty)}{\partial \omega} = -\frac{1}{2}\frac{1}{\sqrt{M_0^2 + k^2 - \omega^2}}, \tag{B5a}$$

$$\frac{\partial \alpha_s(\infty)}{\partial k} = \frac{\omega k - M_0\sqrt{M_0^2 + k^2 - \omega^2}}{\sqrt{M_0^2 + k^2 - \omega^2}}, \tag{B5b}$$

$$\sin 2\alpha_s(\infty) = \frac{M_0\sqrt{M_0^2 + k^2 - \omega^2} - \omega k}{M_0^2 + k^2}. \tag{B5c}$$

Eq. (B4) is then transformed to

$$\frac{\partial\omega}{\partial t}+\left(\frac{M_0\sqrt{M_0^2+k^2-\omega^2}-\omega k}{M_0^2+k^2}\right)\times\left(-\frac{\partial\omega}{\partial x}+\frac{\partial k}{\partial t}-\frac{\partial k}{\partial x}\frac{M_0\sqrt{M_0^2+k^2-\omega^2}-\omega k}{M_0^2+k^2}\right)=0\,. \tag{B6}$$

In the weakly nonlinear regime, $k^2,\omega^2\ll M_0^2$, Eq. (B6) can be simplified by expanding the coefficients into the Taylor series of k/M_0 and ω/M_0. Using the relation (B3), this decomposition up to the quadratic order gives the equation of the nonlinear simple wave for the intensity-dependent dispersion (4):

$$\partial_t(\omega+k)-\left(1-\frac{(\omega+k)^2}{M_0^2}\right)\partial_x(\omega+k)=0, \tag{B7}$$

or equivalently, Eq. (8). Thus, we have shown that the dynamics of the edge pulse in the case of weak focusing ($g>0$) Kerr nonlinearity is described by the nonlinear simple wave equation (8). The key feature of this equation is an intensity-dependent wave speed; the brighter parts of the pulse travel more slowly. Therefore, in the course of propagation, the pulse tail steepens and develops a gradient catastrophe.

The solution of Eq. (8) is the function $\mathcal{I}_1=f(x-v(f)t)$, where profile f is found from the initial condition $f(x,t=0)=f_0(x)$. This solution is applicable up to the gradient catastrophe that occurs when the characteristics overlap. The characteristics constitute a family of curves $x=x'+v(f_0(x'))$, where the prime coordinates x' are the points where the initial distribution was set. On the characteristics the amplitude is constant. Since the velocity $v=v(x')$ is coordinate dependent, there exists a point where the characteristics intersect. Taking the initial distribution $\mathcal{I}_1(x,t=0)=f_0(x)$, we determine the rupture time t_*:

$$t_*=\min_x\left[-\frac{1}{(\partial_{\mathcal{I}_1}v)(\partial_x f_0)}\right]. \tag{B8}$$

Using the expression for the group velocity $v=1-g^2\mathcal{I}_1^2/(4M_0^2)$, which follows form Eq. (8), we calculate a derivative $\partial_{\mathcal{I}_1}v=g^2\mathcal{I}_1/(2M_0^2)$ and substitute it into Eq. (B8):

$$t_*=\min_x\left[-\frac{2M_0^2}{g^2 f_0(x)(\partial_x f_0)}\right]. \tag{B9}$$

Assuming the initial pulse envelope has a Gaussian profile, we obtain Eq. (10). The rupture time diverges in the limits of weak nonlinearity ($gF_0/M_0\to 0$) or broad pulses ($\Lambda\to\infty$).

2. Asymptotic approach

Equation (8) can be alternatively derived using the asymptotic methods in the case of weak nonlinearity. In what follows, we also take into account spatial dispersion effects for a staggered graphene model (see Ref. [55]) by adding off-diagonal second-order derivatives in the spatial coordinates Eq. (11),

$$i\partial_t\mathbf{\Psi}=(\hat{H}_D+\hat{H}_{NL}+\hat{H}_{\rm disp})\mathbf{\Psi}, \tag{B10}$$

and develop a perturbation theory for the problem (B10). In the linear dispersionless case ($g=\eta=0$), the domain wall (3) supports edge modes exponentially localized in the transverse direction, with linear dispersion $\omega=-k$ (assume $M_0>0$). Accordingly, the edge pulse propagating along the domain wall does not diffract and has the form:

$$\mathbf{\Psi}=\begin{pmatrix}\Psi_1^{(0)}\\ \Psi_2^{(0)}\end{pmatrix}=a_0(x+t)e^{-M_0|y|}e^{-i\omega(x+t)}\begin{pmatrix}1\\-1\end{pmatrix}, \tag{B11}$$

where polarization column vector is antisymmetric.

To simplify our derivations, we introduce the functions,

$$\Phi_1=\frac{\Psi_1+\Psi_2}{\sqrt{2}},\quad \Phi_2=\frac{\Psi_1-\Psi_2}{\sqrt{2}}\,. \tag{B12}$$

and rewrite the system (B10) in terms of new variables ($x+t\equiv\xi,t$),

$$i\partial_t\Phi_1+2i\partial_\xi\Phi_1=\partial_y\Phi_2+M\Phi_2-\frac{g}{2}F\Phi_1-\frac{g}{2}G\Phi_2+\eta(-\partial_{yy}\Phi_1+\partial_{\xi\xi}\Phi_1-2i\partial_{\xi y}\Phi_2), \tag{B13a}$$

$$i\partial_t\Phi_2=-\partial_y\Phi_1+M\Phi_1-\frac{g}{2}F\Phi_2-\frac{g}{2}G\Phi_1+\eta(\partial_{yy}\Phi_2-\partial_{\xi\xi}\Phi_2+2i\partial_{\xi y}\Phi_1), \tag{B13b}$$

where $F=|\Phi_1|^2+|\Phi_2|^2$ and $G=\Phi_1\Phi_2^*+\Phi_1^*\Phi_2$. At $g=\eta=0$, according to Eq. (B11), at $\omega=0$ the solution of Eq. (B13) is a column vector

$$\begin{pmatrix}\Phi_1^{(0)}\\ \Phi_2^{(0)}\end{pmatrix}=\begin{pmatrix}0\\ \sqrt{2}\sqrt{\mathcal{I}_1}e^{-M_0|y|}\end{pmatrix}\equiv\begin{pmatrix}0\\ a(\xi)e^{-M_0|y|}\end{pmatrix}. \tag{B14}$$

We assume that nonlinearity is weak ($g\mathcal{I}_1\ll M_0$) and introduce a small parameter $\mu\sim g\mathcal{I}_1/M_0$. Starting from the known linear solution (B14), we look for the solution of Eqs. (B13) in the form of an asymptotic expansion in μ. The influence of spatial dispersion will be accounted in the order $\sim\mu^2$, ($\eta M_0\sim\mu^2$).

$$\Phi_1=\sum_{n=1}^{\infty}\mu^n\Phi_1^{(n)}(y;\xi;\tau_1,\tau_2,\ldots), \tag{B15a}$$

$$\Phi_2=a(\xi;\tau_1,\tau_2,\ldots)e^{-M_0|y|}+\sum_{n=1}^{\infty}\mu^n\Phi_2^{(n)}(y;\xi;\tau_1,\tau_2,\ldots), \tag{B15b}$$

where we used a hierarchy of time scales, $\tau_n=\mu^n t$, according to which $\partial_t a=\mu\partial_{\tau_1}a+\mu^2\partial_{\tau_2}a+\ldots$.

In the first order, $\sim\mu$ Eq. (B13a) at $y>0$ gives

$$\partial_y\Phi_1^{(1)}-M_0\Phi_1^{(1)}=-\frac{g}{2}a|a|^2e^{-3M_0y}-ie^{-M_0y}\partial_{\tau_1}a. \tag{B16}$$

This is a linear inhomogeneous differential equation of the first order. Applying the method of variation of an arbitrary constant, its solution is written as [here, we also use the boundary condition $\Phi_1^{(1)}(y=0)=0$)]:

$$\Phi_1^{(1)}=e^{M_0y}\int_0^y dy'\left(-\frac{g}{2}a|a|^2e^{-4M_0y'}-i\frac{\partial a}{\partial\tau_1}e^{-2M_0y'}\right). \tag{B17}$$

The condition of existence of the localized solution (B17), $\Phi_1^{(1)}(y \to \pm\infty) \to 0$,

$$\int_0^\infty dy' \left(-\frac{g}{2} a|a|^2 e^{-4M_0 y'} - i\frac{\partial a}{\partial \tau_1} e^{-2M_0 y'} \right) = 0 \,,$$

leads to the equation for the amplitude a:

$$i\frac{\partial a}{\partial \tau_1} = -\frac{g}{4}|a|^2 a \,, \tag{B18}$$

which recovers the self-phase modulation arising from the diagonal nonlinear terms. Substituting Eq. (B18) into Eq. (B17) and integrating over y, we obtain the correction $\Phi_1^{(1)}$ to the transverse profile of the first order of smallness:

$$\Phi_1^{(1)} = -\frac{g}{8M_0}|a|^2 a(e^{-M_0 y} - e^{-3M_0 y}) \,. \tag{B19}$$

This intensity-dependent correction results in the uniform y-independent spin of the linear edge state becoming y-dependent.

Next, we consider the second equation (B13b) in the order $\sim\mu^1$,

$$\partial_y \Phi_2^{(1)} + M_0 \Phi_2^{(1)} = 2i\partial_\xi \Phi_1^{(1)}. \tag{B20}$$

The solution of this inhomogeneous equation is as follows:

$$\begin{aligned} \Phi_2^{(1)} &= e^{-M_0 y} \int_0^y dy' \left(2i\frac{\partial \Phi_1^{(1)}}{\partial \xi} \right) e^{M_0 y'} \\ &= \frac{ig}{8M_0^2} \left(\frac{\partial |a|^2 a}{\partial \xi} \right) (e^{-M_0 y} - e^{-3M_0 y} - 2M_0 y e^{-M_0 y}) \,. \end{aligned} \tag{B21}$$

In the second order $\sim\mu^2$, the second equation of the system (B13) leads to

$$\partial_y \Phi_1^{(2)} - M_0 \Phi_1^{(2)} = q(y), \tag{B22}$$

where we denote the right-hand side by $q(y)$,

$$\begin{aligned} q(y) = &- ie^{-M_0 y}\partial_{\tau_2} a - i\partial_{\tau_1} \Phi_2^{(1)} - \frac{g}{2}\big(2|a|^2 \Phi_2^{(1)} \\ &+ a^2 \Phi_2^{(1)*}\big) e^{-2M_0 y} - \eta\big(\partial_{\xi\xi} a - M_0^2 a\big) e^{-M_0 y}, \end{aligned} \tag{B23}$$

and substitute there $\Phi_2^{(1)}$ from Eq. (B21). The solution of Eq. (B22) is $\Phi_1^{(2)} = e^{M_0 y} \int_0^y dy' q(y') e^{-M_0 y'}$. After some transformations, from the condition of localization for the correction $\Phi_1^{(2)}(y \to \pm\infty) \to 0$, i.e., $\int_0^\infty dy' q(y') e^{-M_0 y'} = 0$, we find

$$i\frac{\partial a}{\partial \tau_2} + i\frac{g^2}{32M_0^2} a|a|^2 \frac{\partial |a|^2}{\partial \xi} + \eta \frac{\partial^2 a}{\partial \xi^2} - \eta M_0^2 a = 0. \tag{B24}$$

Neglecting spatial dispersion $\eta = 0$, Eq. (B24) for the magnitude $|a|$ takes a compact form,

$$\frac{\partial |a|}{\partial \tau_2} + \frac{g^2}{16M_0^2}|a|^4 \frac{\partial |a|}{\partial \xi} = 0, \tag{B25}$$

that, bearing in mind $\sqrt{2\mathcal{I}_1} \equiv |a|$ and $\xi \equiv x + t$, fully coincides with Eq. (8).

Summing up Eqs. (B18) and (B24) and replacing $\mu\partial_{\tau_1} + \mu^2\partial_{\tau_2} \to \partial_t$, we obtain the evolution equation (12) for the edge pulse with accuracy $\sim\mu^2$.

By substituting approximate expansions $\Phi_{1,2} = \Phi_{1,2}^{(0)} + \Phi_{1,2}^{(1)}$ with the use of expressions (B14), (B19), (B21) into the definitions of the integral characteristics (5) rewritten through $\Phi_{1,2}$,

$$\mathcal{P} = \int_0^\infty (|\Phi_1|^2 + |\Phi_2|^2) dy \,, \tag{B26a}$$

$$S_x = \frac{1}{2}\int_0^\infty (|\Phi_1|^2 - |\Phi_2|^2) dy \,. \tag{B26b}$$

Eq. (B25) is recovered directly from Eq. (7), which constitutes the the exact property of transversely localized solutions in the NDM at $\eta = 0$.

3. Edge solitons

Equation (12) is invariant with respect to Galilean transformation $a(\xi, t) \to \tilde{a}(\zeta, t) \exp(i\frac{v}{2\eta}\xi + i\frac{v^2}{4\eta}t)$, where $\zeta = \xi - vt$:

$$i\frac{\partial \tilde{a}}{\partial t} \approx -\frac{g}{4}|\tilde{a}|^2\tilde{a} - i\frac{g^2}{32M_0^2}|\tilde{a}|^2\frac{\partial |\tilde{a}|^2}{\partial \zeta}\tilde{a} - \eta\frac{\partial^2 \tilde{a}}{\partial \zeta^2} + M_0^2\eta\tilde{a}. \tag{B27}$$

Note, considering the applicability of the approximations employed for derivation of Eq. (12), the velocity in the Galilean transformation is small, $v \lesssim \mu^2$.

We look for the soliton solution of Eq. (B27) of the form $\tilde{a} = \mathcal{A}(\zeta)e^{-i\omega_s t + i\varphi(\zeta)}$, where $\mathcal{A}(\zeta \to \pm\infty) \to 0$ is a real-valued localized function, and separate imaginary and real parts of Eq. (B27),

$$\frac{g^2}{16M_0^2}\mathcal{A}^4\frac{\partial \mathcal{A}}{\partial \zeta} + \eta(2\partial_\zeta \mathcal{A}\partial_\zeta \varphi + \mathcal{A}\partial_{\zeta\zeta}\varphi) = 0 \,, \tag{B28a}$$

$$\omega_s \mathcal{A} - \eta M_0^2 \mathcal{A} + \frac{g}{4}\mathcal{A}^3 + \eta(\partial_{\zeta\zeta}\mathcal{A} - (\partial_\zeta \varphi)^2 \mathcal{A}) = 0 \,. \tag{B28b}$$

Next, we multiply Eq. (B28a) by $\mathcal{A}$ and integrate over y from $-\infty$ to ζ:

$$\frac{\partial \varphi}{\partial \zeta} = -\frac{g^2\mathcal{A}^4}{96M_0^2\eta} \,. \tag{B29}$$

Hence, we find the phase

$$\varphi = -\frac{g^2}{96M_0^2\eta}\int_{-\infty}^{\zeta} \mathcal{A}^4(\zeta')d\zeta' \tag{B30}$$

and substitute its derivative (B29) into Eq. (B28b):

$$\mathcal{A}'' = -\left(\frac{\omega_s}{\eta} - M_0^2\right)\mathcal{A} - \frac{g}{4\eta}\mathcal{A}^3 + \frac{g^4}{96^2\eta^2 M_0^4}\mathcal{A}^9. \tag{B31}$$

Eq. (B31) can be integrated, since it obeys the form $\mathcal{A}'' = -\frac{\partial U(\mathcal{A})}{\partial \mathcal{A}}$ with potential U given by

$$U = \left(\frac{\omega_s}{\eta} - M_0^2\right)\frac{\mathcal{A}^2}{2} + \frac{g}{4\eta}\frac{\mathcal{A}^4}{4} - \frac{g^4}{96^2\eta^2 M_0^4}\frac{\mathcal{A}^{10}}{10}. \tag{B32}$$

The soliton solution corresponds to a separatrix of the saddle steady state located at the point (0,0) in the phase plane $(\mathcal{A}', \mathcal{A})$, which exists at $(\omega_s/\eta - M_0^2) < 0$. Note, under our approximations which warrant applicability of Eq. (B31), the last nonlinear term in Eq. (B31) should be small compared to

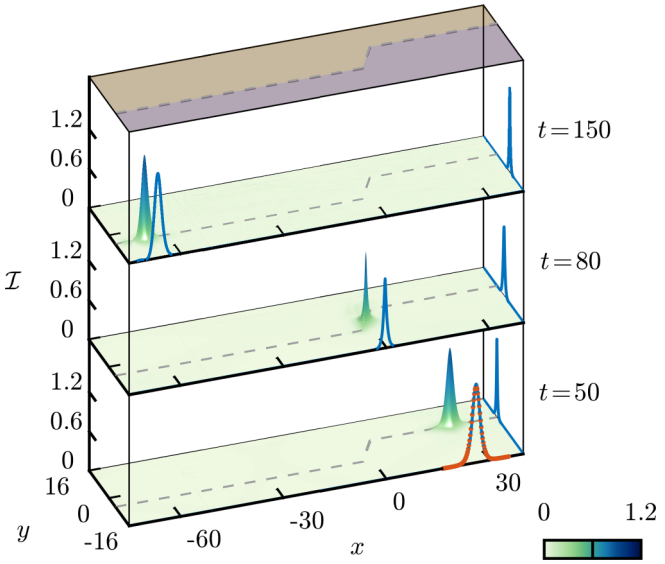

FIG. 7. Edge soliton propagating along the domain wall and bypassing corners. Slices show snapshots of the intensity distribution $\mathcal{I}(x, y)$ at $t = 50$ (bottom), $t = 80$ (middle), $t = 150$ (top). The shifted initial soliton envelope of maximum intensity 1.2 at $\omega_s = 0.02$ is overlaid with red dots at (at the bottom slice). Parameters are $M_0 = 1$, $g = 0.125$, $\eta = 0.05$.

the cubic one. Therefore, the soliton of Eq. (B31) is topologically close to the soliton of the conventional NLSE, obtained by omitting the last term $\propto g^4$, i.e.,

$$\mathcal{A}'' = -\left(\frac{\omega_s}{\eta} - M_0^2\right)\mathcal{A} - \frac{g}{4\eta}\mathcal{A}^3, \tag{B33}$$

which has a well-known analytical solution:

$$\mathcal{A} = \frac{\sqrt{8\left(M_0^2\eta - \omega_s\right)/g}}{\cosh\left(\zeta\sqrt{M_0^2 - \omega_s/\eta}\right)}. \tag{B34}$$

Stable soliton propagation and its ability to traverse corners is illustrated in Fig. 7.

APPENDIX C: PARAXIAL MODELING

To model a realistic lattice of laser-written waveguides, we employ the paraxial equation for the electric field $\mathcal{E}$,

$$i\frac{\partial\mathcal{E}}{\partial z} + \frac{1}{2k_0}\Delta_\perp\mathcal{E} + \frac{k_0(n_L(x,y) + n_2|\mathcal{E}|^2)}{n_0}\mathcal{E} = 0, \tag{C1}$$

where z is the propagation coordinate, (x, y) are the transverse coordinates, λ is the vacuum wavelength, $k_0 = 2\pi n_0/\lambda$ is the wavenumber, and n_0 is the background refractive index. The staggered graphene lattice is imprinted in distribution of the linear refractive index $n_L(x, y) = n_A\sum_{n,m} S(x - x_n, y - y_m) + n_B\sum_{n,m} S(x - x_n, y - y_m)$, where summation is performed over the the lattice sites with coordinates x_n, y_m. Two triangular sublattices are indexed with subscripts A and B; n_A and n_B refer to perturbations of the refractive index in waveguides. The elliptical waveguides have the Gaussian shape with semiaxes a_x, a_y, described by function $S(x, y) = e^{-x^2/a_x^2 - y^2/a_y^2}$. The nonlinear term $\propto n_2|\mathcal{E}|^2\mathcal{E}$ is responsible for a focusing cubic nonlinearity. A schematic of the lattice stripe

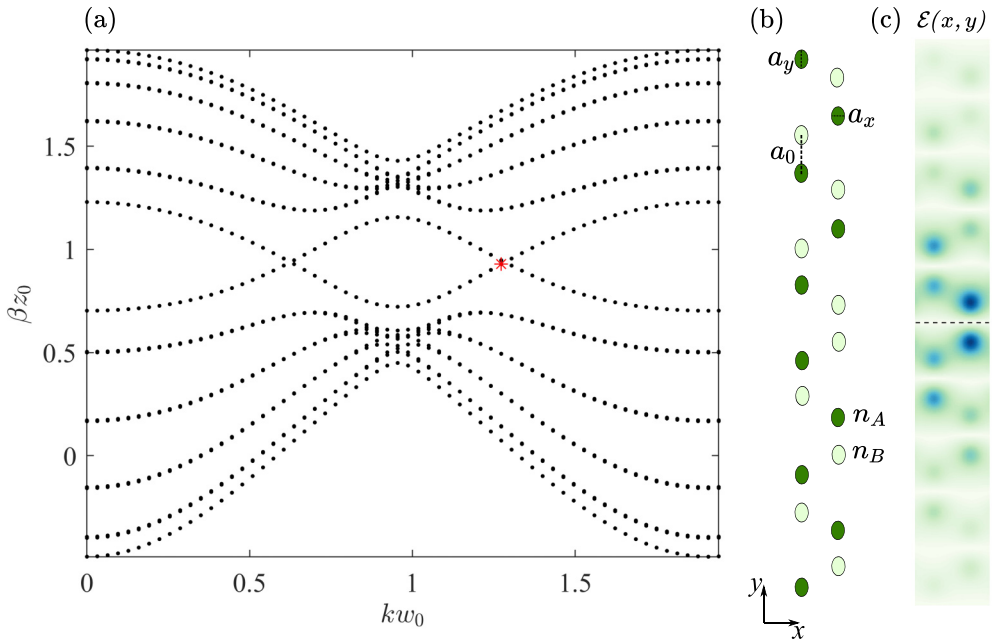

FIG. 8. (a) Band structure $\beta(k)$ for a supercell of the staggered graphene lattice, composed of 20 dielectric elliptical waveguides with semiaxes a_x, a_y, as illustrated in (b). Normalization length parameters are $w_0 = 10$ μm, $z_0 = 2k_0w_0^2$. Dark green and light green colors in (b) correspond to two different perturbations of the refractive index n_A, n_B, respectively, in a bipartite lattice. (c) Profile of the stationary edge state $\mathcal{E}(x, y)$, with the wave number spotted with a red asterisk in (a). Gray dashed line in (c) locates the interfacial domain wall.

TABLE I. Parameters of the waveguide lattice used in modeling.

Parameter	Value
a_x	$3.2\,\mu$m
a_y	$4.9\,\mu$m
a_0	$19\,\mu$m
n_0	1.47
n_A	2.6×10^{-3}
n_B	2.8×10^{-3}
n_2	$3 \times 10^{-20}\,\mathrm{m}^2/\mathrm{W}$
λ	1650 nm
I_0	$10^{16}\,\mathrm{W}/\mathrm{m}^2$

incorporating zigzag domain walls is shown in Fig. 8 with parameters listed in Table I.

Linear modes (at $n_2 = 0$), being Bloch states $\mathcal{E} = u(x, y)e^{i\beta z + ikx}$, are obtained from the eigenvalue problem

$$\beta u = \frac{1}{2k_0}\left((\partial_x + ik)^2 + \partial_y^2\right)u + \frac{k_0}{n_0}n_L(x, y)u, \tag{C2}$$

which is solved numerically for spectrum $\beta(k)$ in the configuration of Fig. 8(b) by using the plane-wave expansion method. Periodic boundary conditions are applied to the stripe in the lateral directions. The valley edge states, which localize at the domain walls, exhibit Dirac-like dispersion crossings at two valleys; see Fig. 8(a). The calculated edge mode profile 8(c) is then used in setting the initial field distribution for the beam evolution modeling displayed in Fig. 5.

Paraxial equation can be mapped onto the tight-binding model [16,61,62] with effective parameters $\kappa = 3.47\ \mathrm{cm}^{-1}$, $M_0 = 1.73\ \mathrm{cm}^{-1}$ reconstructed from matching the band structures in different models and nonlinear coefficient $g = n_2 k_0/n_0$. The transition to the continuum limit from the valley-Hall lattice model we used to substantiate the Dirac model is described in detail in Refs. [23,55,56].

[1] D. Smirnova, D. Leykam, Y. Chong, and Y. Kivshar, Nonlinear topological photonics, Appl. Phys. Rev. **7**, 021306 (2020).

[2] A. Saxena, P. G. Kevrekidis, and J. Cuevas-Maraver, *Nonlinearity and Topology* (Springer International Publishing, Cham, 2020), pp. 25–54.

[3] W. Chen, D. Leykam, Y. Chong, and L. Yang, Nonreciprocity in synthetic photonic materials with nonlinearity, MRS Bulletin **43**, 443 (2018).

[4] D. A. Dobrykh, A. V. Yulin, A. P. Slobozhanyuk, A. N. Poddubny, and Y. S. Kivshar, Nonlinear Control of Electromagnetic Topological Edge States, Phys. Rev. Lett. **121**, 163901 (2018).

[5] M. I. Shalaev, W. Walasik, and N. M. Litchinitser, Optically tunable topological photonic crystal, Optica **6**, 839 (2019).

[6] S. Kruk, A. Poddubny, D. Smirnova, L. Wang, A. Slobozhanyuk, A. Shorokhov, I. Kravchenko, B. Luther-Davies, and Y. Kivshar, Nonlinear light generation in topological nanostructures, Nat. Nanotechnol. **14**, 126 (2019).

[7] D. Smirnova, S. Kruk, D. Leykam, E. Melik-Gaykazyan, D.-Y. Choi, and Y. Kivshar, Third-Harmonic Generation in Photonic Topological Metasurfaces, Phys. Rev. Lett. **123**, 103901 (2019).

[8] S. Mittal, E. A. Goldschmidt, and M. Hafezi, A topological source of quantum light, Nature (London) **561**, 502 (2018).

[9] Y. Wang, L.-J. Lang, C. H. Lee, B. Zhang, and Y. D. Chong, Topologically enhanced harmonic generation in a nonlinear transmission line metamaterial, Nat. Commun. **10**, 1102 (2019).

[10] Y. Zeng, U. Chattopadhyay, B. Zhu, B. Qiang, J. Li, Y. Jin, L. Li, A. G. Davies, E. H. Linfield, B. Zhang, Y. Chong, and Q. J. Wang, Electrically pumped topological laser with valley edge modes, Nature (London) **578**, 246 (2020).

[11] Z. Lan, J. W. You, and N. C. Panoiu, Nonlinear one-way edge-mode interactions for frequency mixing in topological photonic crystals, Phys. Rev. B **101**, 155422 (2020).

[12] T. Ma and G. Shvets, All-Si valley-Hall photonic topological insulator, New J. Phys. **18**, 025012 (2016).

[13] X.-D. Chen, F.-L. Zhao, M. Chen, and J.-W. Dong, Valley-contrasting physics in all-dielectric photonic crystals: Orbital angular momentum and topological propagation, Phys. Rev. B **96**, 020202(R) (2017).

[14] J.-W. Dong, X.-D. Chen, H. Zhu, Y. Wang, and X. Zhang, Valley photonic crystals for control of spin and topology, Nat. Mater. **16**, 298 (2017).

[15] X. Wu, Y. Meng, J. Tian, Y. Huang, H. Xiang, D. Han, and W. Wen, Direct observation of valley-polarized topological edge states in designer surface plasmon crystals, Nat. Commun. **8**, 1304 (2017).

[16] J. Noh, S. Huang, K. P. Chen, and M. C. Rechtsman, Observation of Photonic Topological Valley Hall Edge States, Phys. Rev. Lett. **120**, 063902 (2018).

[17] X. Ni, D. Purtseladze, D. A. Smirnova, A. Slobozhanyuk, A. Alù, and A. B. Khanikaev, Spin- and valley-polarized one-way Klein tunneling in photonic topological insulators, Sci. Adv. **4**, eaap8802 (2018).

[18] X.-D. Chen, F.-L. Shi, H. Liu, J.-C. Lu, W.-M. Deng, J.-Y. Dai, Q. Cheng, and J.-W. Dong, Tunable Electromagnetic Flow Control in Valley Photonic Crystal Waveguides, Phys. Rev. Appl. **10**, 044002 (2018).

[19] Y. Kang, X. Ni, X. Cheng, A. B. Khanikaev, and A. Z. Genack, Pseudo-spin–valley coupled edge states in a photonic topological insulator, Nat. Commun. **9**, 3029 (2018).

[20] F. Gao, H. Xue, Z. Yang, K. Lai, Y. Yu, X. Lin, Y. Chong, G. Shvets, and B. Zhang, Topologically protected refraction of robust kink states in valley photonic crystals, Nat. Phys. **14**, 140 (2018).

[21] M. I. Shalaev, W. Walasik, A. Tsukernik, Y. Xu, and N. M. Litchinitser, Robust topologically protected transport in photonic crystals at telecommunication wavelengths, Nat. Nanotechnol. **14**, 31 (2018).

[22] X.-T. He, E.-T. Liang, J.-J. Yuan, H.-Y. Qiu, X.-D. Chen, F.-L. Zhao, and J.-W. Dong, A silicon-on-insulator slab for topological valley transport, Nat. Commun. **10**, 872 (2019).

[23] D. Smirnova, A. Tripathi, S. Kruk, M.-S. Hwang, H.-R. Kim, H.-G. Park, and Y. Kivshar, Room-temperature lasing from

nanophotonic topological cavities, Light Sci. Appl. **9**, 127 (2020).

[24] Y. Yang, Y. Yamagami, X. Yu, P. Pitchappa, J. Webber, B. Zhang, M. Fujita, T. Nagatsuma, and R. Singh, Terahertz topological photonics for on-chip communication, Nat. Photonics **14**, 446 (2020).

[25] J. Guglielmon and M. C. Rechtsman, Broadband Topological Slow Light Through Higher Momentum-Space Winding, Phys. Rev. Lett. **122**, 153904 (2019).

[26] E. Sauer, J. P. Vasco, and S. Hughes, Theory of intrinsic propagation losses in topological edge states of planar photonic crystals, Phys. Rev. Res. **2**, 043109 (2020).

[27] G. Arregui, J. Gomis-Bresco, C. M. Sotomayor-Torres, and P. D. Garcia, Quantifying the Robustness of Topological Slow Light, Phys. Rev. Lett. **126**, 027403 (2021).

[28] D. Anderson and M. Lisak, Nonlinear asymmetric self-phase modulation and self-steepening of pulses in long optical waveguides, Phys. Rev. A **27**, 1393 (1983).

[29] N. C. Panoiu, X. Liu, and R. M. Osgood, Self-steepening of ultrashort pulses in silicon photonic nanowires, Opt. Lett. **34**, 947 (2009).

[30] J. C. Travers, W. Chang, J. Nold, N. Y. Joly, and P. S. J. Russell, Ultrafast nonlinear optics in gas-filled hollow-core photonic crystal fibers, J. Opt. Soc. Am. B **28**, A11 (2011).

[31] C. Husko and P. Colman, Giant anomalous self-steepening in photonic crystal waveguides, Phys. Rev. A **92**, 013816 (2015).

[32] Y. Kivshar and G. Agrawal, *Optical Solitons: From Fibers to Photonic Crystals* (Elsevier, 2003).

[33] M. Soljačić and J. D. Joannopoulos, Enhancement of nonlinear effects using photonic crystals, Nat. Mater. **3**, 211 (2004).

[34] J. M. Dudley, G. Genty, and S. Coen, Supercontinuum generation in photonic crystal fiber, Rev. Mod. Phys. **78**, 1135 (2006).

[35] Y. Lumer, Y. Plotnik, M. C. Rechtsman, and M. Segev, Self-Localized States in Photonic Topological Insulators, Phys. Rev. Lett. **111**, 243905 (2013).

[36] Y. V. Kartashov and D. V. Skryabin, Modulational instability and solitary waves in polariton topological insulators, Optica **3**, 1228 (2016).

[37] D. Leykam and Y. D. Chong, Edge Solitons in Nonlinear-Photonic Topological Insulators, Phys. Rev. Lett. **117**, 143901 (2016).

[38] D. Solnyshkov, O. Bleu, B. Teklu, and G. Malpuech, Chirality of Topological Gap Solitons in Bosonic Dimer Chains, Phys. Rev. Lett. **118**, 023901 (2017).

[39] W. Zhang, X. Chen, Y. V. Kartashov, V. V. Konotop, and F. Ye, Coupling of Edge States and Topological Bragg Solitons, Phys. Rev. Lett. **123**, 254103 (2019).

[40] T. Tuloup, R. W. Bomantara, C. H. Lee, and J. Gong, Nonlinearity induced topological physics in momentum space and real space, Phys. Rev. B **102**, 115411 (2020).

[41] R. Chaunsali, H. Xu, J. Yang, P. G. Kevrekidis, and G. Theocharis, Stability of topological edge states under strong nonlinear effects, Phys. Rev. B **103**, 024106 (2021).

[42] M. Guo, S. Xia, N. Wang, D. Song, Z. Chen, and J. Yang, Weakly nonlinear topological gap solitons in Su–Schrieffer–Heeger photonic lattices, Opt. Lett. **45**, 6466 (2020).

[43] S. Xia, D. Jukić, N. Wang, D. Smirnova, L. Smirnov, L. Tang, D. Song, A. Szameit, D. Leykam, J. Xu, Z. Chen, and H. Buljan, Nontrivial coupling of light into a defect: The interplay of nonlinearity and topology, Light Sci. Appl. **9**, 147 (2020).

[44] S. Mukherjee and M. C. Rechtsman, Observation of Floquet solitons in a topological bandgap, Science **368**, 856 (2020).

[45] L. J. Maczewsky, M. Heinrich, M. Kremer, S. K. Ivanov, M. Ehrhardt, F. Martinez, Y. V. Kartashov, V. V. Konotop, L. Torner, D. Bauer, and A. Szameit, Nonlinearity-induced photonic topological insulator, Science **370**, 701 (2020).

[46] M. J. Ablowitz, C. W. Curtis, and Y. Zhu, Localized nonlinear edge states in honeycomb lattices, Phys. Rev. A **88**, 013850 (2013).

[47] M. J. Ablowitz, C. W. Curtis, and Y.-P. Ma, Linear and nonlinear traveling edge waves in optical honeycomb lattices, Phys. Rev. A **90**, 023813 (2014).

[48] Y. Lumer, M. C. Rechtsman, Y. Plotnik, and M. Segev, Instability of bosonic topological edge states in the presence of interactions, Phys. Rev. A **94**, 021801(R) (2016).

[49] S. K. Ivanov, Y. V. Kartashov, A. Szameit, L. Torner, and V. V. Konotop, Vector topological edge solitons in Floquet insulators, ACS Photonics **7**, 735 (2020).

[50] S. K. Ivanov, Y. V. Kartashov, L. J. Maczewsky, A. Szameit, and V. V. Konotop, Bragg solitons in topological Floquet insulators, Opt. Lett. **45**, 2271 (2020).

[51] J. Cuevas-Maraver, P. G. Kevrekidis, A. Saxena, A. Comech, and R. Lan, Stability of Solitary Waves and Vortices in a 2D Nonlinear Dirac Model, Phys. Rev. Lett. **116**, 214101 (2016).

[52] R. W. Bomantara, W. Zhao, L. Zhou, and J. Gong, Nonlinear Dirac cones, Phys. Rev. B **96**, 121406(R) (2017).

[53] H. Sakaguchi and B. A. Malomed, One- and two-dimensional gap solitons in spin-orbit-coupled systems with Zeeman splitting, Phys. Rev. A **97**, 013607 (2018).

[54] A. N. Poddubny and D. A. Smirnova, Ring Dirac solitons in nonlinear topological systems, Phys. Rev. A **98**, 013827 (2018).

[55] D. A. Smirnova, L. A. Smirnov, D. Leykam, and Y. S. Kivshar, Topological edge states and gap solitons in the nonlinear Dirac model, Laser Photonics Rev. **13**, 1900223 (2019).

[56] X. Ni, D. Smirnova, A. Poddubny, D. Leykam, Y. Chong, and A. B. Khanikaev, $\mathcal{PT}$ phase transitions of edge states at $\mathcal{PT}$ symmetric interfaces in non-Hermitian topological insulators, Phys. Rev. B **98**, 165129 (2018).

[57] G. W. Semenoff, V. Semenoff, and F. Zhou, Domain Walls in Gapped Graphene, Phys. Rev. Lett. **101**, 087204 (2008).

[58] W. Yao, S. A. Yang, and Q. Niu, Edge States in Graphene: From Gapped Flat-Band to Gapless Chiral Modes, Phys. Rev. Lett. **102**, 096801 (2009).

[59] D. Leykam, E. Smolina, A. Maluckov, S. Flach, and D. A. Smirnova, Probing Band Topology Using Modulational Instability, Phys. Rev. Lett. **126**, 073901 (2021).

[60] N. Pernet, P. St-Jean, D. D. Solnyshkov, G. Malpuech, N. C. Zambon, B. Real, O. Jamadi, A. Lemaître, M. Morassi, L. L. Gratiet, T. Baptiste, A. Harouri, I. Sagnes, A. Amo, S. Ravets, and J. Bloch, Topological gap solitons in a 1D non-Hermitian lattice, arXiv:2101.01038 (2021).

[61] A. Szameit, D. Blömer, J. Burghoff, T. Pertsch, S. Nolte, and A. Tünnermann, Hexagonal waveguide arrays written with fs-laser pulses, Appl. Phys. B **82**, 507 (2006).

[62] J. Noh, W. A. Benalcazar, S. Huang, M. J. Collins, K. P. Chen, T. L. Hughes, and M. C. Rechtsman, Topological protection of photonic mid-gap defect modes, Nat. Photonics **12**, 408 (2018).